High-resolution observations of the North Pacific transition layer from a Lagrangian float

Alexis K. Kaminski*

Department of Mechanical Engineering, University of California, Berkeley, Berkeley, California

Eric A. D'Asaro, Andrey Y. Shcherbina, Ramsey R. Harcourt

Applied Physics Laboratory, University of Washington, Seattle, Washington

**Corresponding author*: Alexis Kaminski, kaminski@berkeley.edu

ABSTRACT

A crucial region of the ocean surface boundary layer (OSBL) is the strongly-sheared and -stratified transition layer (TL) separating the mixed layer from the upper pycnocline, where a diverse range of waves and instabilities are possible. Previous work suggests that these different waves and instabilities will lead to different OSBL behaviours. Therefore, understanding which physical processes occur is key for modelling the TL. Here we present observations of the TL from a Lagrangian float deployed for 73 days near Ocean Weather Station Papa (50°N, 145°W) during Fall 2018. The float followed the vertical motion of the TL, continuously measuring profiles across it using an ADCP, temperature chain and salinity sensors. The temperature chain made depth/time images of TL structures with a resolution of 6cm and 3 seconds. These showed the frequent occurrence of very sharp interfaces, dominated by temperature jumps of O(1)°C over 6cm or less. Temperature inversions were typically small ($\lesssim$ 10cm), frequent, and strongly-stratified; very few large overturns were observed. The corresponding velocity profiles varied over larger length scales than the temperature profiles. These structures are consistent with Holmboe-like scouring behaviour rather than Kelvin-Helmholtz-type overturning. Their net effect, estimated via a Thorpe-scale analysis, suggests that these frequent small temperature inversions can account for the observed mixed layer deepening and entrainment flux. Corresponding estimates of dissipation, diffusivity, and heat fluxes also agree with previous TL studies, suggesting that the TL dynamics is dominated by these nearly continuous 10cm-scale mixing structures, rather than by less frequent larger overturns.

1. Introduction

The ocean surface boundary layer (OSBL) plays an important role in the global climate system, mediating exchanges of heat, momentum, and trace gases between the atmosphere and stably-stratified ocean interior (Ferrari and Boccaletti 2004) and controlling ocean primary productivity through access to light and nutrients (Archer 1995; Mahadevan 2016). Accurately representing the depth and structure of this layer is therefore key in large-scale climate and biogeochemical models. However, models often exhibit large errors of both signs in mixed layer depth (Belcher et al. 2012; Huang et al. 2014; Li et al. 2019). One possible reason for these discrepancies is in the parameterization of the small-scale physics underlying vertical mixing. As such, understanding the dynamics driving entrainment and mixing in the OSBL is a fundamental problem in modelling the upper ocean.

The OSBL consists of a well-mixed turbulent upper layer overlying a strongly-sheared, strongly-stratified "transition layer" (TL). Mixed layer (ML) turbulence is generated by the action of wind, waves, and surface buoyancy fluxes, with the details of the flow depending on the balance of the different forcings. For example, strong destabilizing surface buoyancy fluxes drive convective turbulence characterized by narrow downward plumes of dense, cold fluid (Deardorff 1970; Harcourt et al. 2002), while wind-driven shear plays a larger role in driving ML turbulence under weakly convective, neutral, or stabilizing surface fluxes (Niiler 1975; Price 1979; Gargett et al. 1979). In addition, surface waves play an important role in ML dynamics: not only does wave breaking drive energetic turbulence near the surface (Agrawal et al. 1992), but the interaction between Stokes drift and Eulerian currents can drive Langmuir flows, leading to turbulence with stronger vertical fluctuations and higher mixing rates (Craik and Leibovich 1976; D'Asaro 2014).

While the description of ML dynamics has improved significantly in recent years, our understanding of the behaviour of the transition layer is less well developed. The TL is characterized by strong shear and stratification, with elevated turbulent dissipation rates compared to the upper thermocline (Sun et al. 2013). The associated turbulent mixing and entrainment may arise from a wide variety of physical processes, both internally- and externally-generated (Johnston and Rudnick 2009). For instance, the strong stratification can support internal waves, which receive energy from the ML, transport it, and drive local mixing where they break. Shear instabilities can also be triggered by strong vertical shears at the ML base, driving turbulent mixing and entrainment of denser fluid from the interior. In addition to locally-generated turbulence, the TL may also interact with the turbulent ML, either via vertical heaving of the mixed layer base (bringing denser isopycnals into contact with ML turbulence) or vertical flows associated with convective or Langmuir turbulence impinging on the TL from above. These different processes may also work concurrently; for example, Langmuir circulations may enhance shear at the ML base, facilitating entrainment and deepening (Kukulka et al. 2010).

Mixing across stratified interfaces depends sensitively on the underlying mechanism (Hannoun and List 1988; Strang and Fernando 2001), and therefore on the details of the shear and stratification. In the idealized case of two well-mixed fluid layers separated by a stratified interface, there are two limiting regimes describing interfacial mixing and entrainment (Strang and Fernando 2001; Woods et al. 2010; Salehipour et al. 2016; Caulfield 2021; Smith et al. 2021). In "overturning" flows, such as those arising from Kelvin-Helmholtz (KH) instability, turbulence broadens the interface and smears out the initial stratification. However, for more strongly-stratified interfaces, this broadening behaviour may give way to scouring, in which turbulent motions adjacent to an interface maintain a sharp stratification. Such scouring motions may arise locally from Holmboe-type instabilities when the shear is broader than the stratification (Carpenter et al. 2007; Salehipour et al. 2016), or from the interaction of the interface with externally-generated turbulence (Fernando 1991). In either case, turbulent vortices entrain wisps of fluid from the interface and mix them into the ambient while keeping the interface sharp (Strang and Fernando 2001; Carpenter et al. 2007; Zhou et al. 2017). Understanding which of these qualitatively different behaviours is at play in a given flow is key to accurately describing the mixing and entrainment.

Ocean observations further suggest that different types of instabilities lead to different OSBL behaviours. For example, Dohan and Davis (2010) examine two storms with similar maximum wind stresses but very different OSBL responses associated with different mean shears across the TL. In the former storm, the mean shear was weak, implying that the TL was stable to shear instability and the dynamics were driven by ML turbulence; correspondingly, the ML deepens and the TL remains approximately the same thickness. Conversely, the latter storm was associated with little change in ML depth but a broadening of the TL, consistent with stronger shears driving shear instabilities. Clearly, accurately identifying the physical processes at play in the TL is critical for understanding and parameterizing the entrainment.

Directly observing these processes is complicated by the transient and intermittent nature of stratified turbulence. To overcome this challenge, here we present observations of the transition layer during the Fall 2018 ML deepening season in the northeast Pacific Ocean, measured from a transition layer float (TLF). This set of observations includes a combination of vertical profiles of the upper ocean (allowing for observation of the overall OSBL structure) and Lagrangian measurements within the TL over more than two months, providing both a vertical and temporal description of TL dynamics. In section 2, we describe the observational study, including the float instrumentation. In section a, we present observations of the temperature, salinity, stratification, and shear of the ocean surface boundary layer down to approximately 120 m depth. Then, in sections b and c, we show the corresponding TL temperature structure from thermistor chain measurements with a vertical resolution of 6 cm and a temporal resolution of 3 s, and show that a multitude of $O(10)$ cm features exist in this region. We relate the observed small-scale features to the overall ML deepening and associated heat fluxes in sections d and e. Finally, in section 4 we conclude and discuss directions for future analysis of this dataset.

2. Observational study

a. Transition layer float

The TLF (Fig. 1a), is based on previous generations of the Applied Physics Laboratory Lagrangian floats (D'Asaro 2003, 2018), and is equipped with a variety of sensors that measured temperature, salinity, and relative velocity throughout the float deployment.

Two SeaBird 41CT conductivity/temperature sensors were mounted on the top and bottom of the float hull measuring every 30 s, allowing the float to target a given isopycnal during the deployment. In addition, the CTD measurements were used to provide information about the local $T-S$ relationship and to enable the calculation of the potential density ρ in the transition layer (section a and appendix 6).

Inspired by the high-resolution shear instability measurements of van Haren and Gostiaux (2010) and van Haren et al. (2014), the TLF was equipped with a pair of thermistor chains, each consisting of 24 RBR thermistors with a vertical spacing of 6 cm, measuring temperature at $1/3$ Hz with an accuracy of 0.001°C. These were embedded in a titanium and syntactic foam structure and mounted to the either side of the float. The T-chains allowed for measurement of both the detailed vertical structure and the temporal evolution of the transition layer temperature field. One of the chains failed partway through the deployment, while the other was able to sample throughout the entire 73 days. The T-chain measurements were intercalibrated using observed temperature values within the mixed layer and the CTD temperature measurements.

A pair of Nortek Signature1000 1 MHz 5-beam ADCPs were attached to either side of the float hull, one looking upward and one downward. The ADCPs alternated between a high-resolution (HR) pulse-pulse coherent sampling mode (giving 3 cm bins) and a long-range (LR) broadband mode (giving 1 m bins), as described in more detail by Shcherbina et al. (2018). Unfortunately, the downlooking ADCP broke shortly into the deployment. The uplooking ADCP fared better, giving good LR velocity measurements at a rate of 1 Hz throughout the 73-day deployment. The HR measurements experienced further difficulties due to contamination by reflections off the float body and previous ping interference; as such, we focus here on the LR measurements and leave analysis of the HR measurements to future work.

b. Details of deployment

The TLF was deployed in the northeastern Pacific about 56 km southeast of NOAA Ocean Weather Station Papa (50°N, 145°W) and drifted approximately 185 km eastward during the deployment. This region, with its strong winds and weak lateral variability and mesoscale activity, is ideal for studies of vertical boundary layer physics as the mixed layer dynamics are close to one-dimensional (Pelland et al. 2016). The float was deployed from 21 September 2018 to 2 December 2018, during the fall mixed layer deepening period. During this time, climatological measurements show a shift from net surface warming to net surface cooling, an increase in surface wind forcing, and the occurrence of several strong storms, leading to an expected overall ML deepening from approximately 20 m to 60 m (Li et al. 2005; Cronin et al. 2015).

The float behaviour is illustrated schematically in Fig. 1(b). Twice daily, the float surfaced for communications and then profiled down to approximately 120 m depth. Then, the float rose to a specific isopycnal chosen to be $0.17\,\mathrm{kg\,m^{-3}}$ denser than the mixed layer. After reaching that isopycnal, the float then drifted for 4000 s, after which point it moved to a new isopycnal $0.1\,\mathrm{kg\,m^{-3}}$ heavier and drifted again. This stepped pattern was repeated until the next surfacing. In doing so, the float was able to sample different parts of the transition layer in each half-day drifting period.

c. Mooring data

In addition to the float measurements, data from NOAA-PMEL Ocean Weather Station Papa were used. The mooring measures a variety of oceanic and meteorological variables, including upper ocean temperature and conductivity, wind speeds, precipitation, and incident radiation. We also make use of bulk air-sea fluxes computed from the observed meteorological and oceanic quantities using the COARE 3.0b algorithm (Fairall et al. 2003; Cronin et al. 2006).

3. Results

a. OSBL structure

We first consider the atmospheric forcing and OSBL structure measured at OWS Papa. Details of the wind stress magnitude $|\boldsymbol{\tau}|$, wind stress direction, and net surface heating q_{net} throughout the deployment are shown in Fig. 2. In addition, the upper ocean density structure at OWS Papa, collected at 13 depths over the upper 200 m, is shown. In early autumn, the surface winds are relatively low until approximately yearday 285 (Fig. 2a,b). At the same time, while the diurnal cycle is apparent, the surface is heated on average (Fig. 2c). During this period, there is little overall change in the upper ocean potential density (Fig. 2d). After approximately yearday 290 (Oct. 17), however, there is a shift towards higher winds and net surface cooling, consistent with climatology. Correspondingly, the mixed layer deepens and becomes denser during the latter part of the float deployment.

We now turn our attention to the upper ocean structure measured during the float's twice-daily profiles of the mixed layer and upper pycnocline (Fig. 1b). Several features are immediately apparent when examining individual profiles of temperature T, salinity S, and potential density ρ (Fig. 3a-c). Both temperature and salinity, and therefore potential density, are overall stably-stratified with a very clear mixed layer overlying a strongly-stratified transition layer in the upper part of the profiles. The thermal stratification decreases with depth below the strong temperature gradient at the ML base. In contrast, while there is a sharp change in salinity immediately below the ML, the vertical gradient below that is weaker and increases with depth. The combined vertical structure of T and S leads to a relatively uniform potential density stratification below the initial sharp change at the ML base. The profiles of T and S also show that the observed changes in ρ are primarily temperature-driven: the mixed layer cools more than 2.5°C in the latter part of the season, while the mixed layer salinity varies by less than 0.1 psu over the entire observation period. This is also apparent in the overall temperature-salinity relationship for the full deployment (appendix 6). We note that density within the TL can be predicted by linear fits to temperature in each Lagrangian drift period with rms errors$< 0.02\,\mathrm{kg\,m^{-3}}$ and $R^2 > 0.99$.

The overall upper ocean potential density evolution is shown in Fig. 3(d). Also plotted is the mixed layer depth, defined here as the first depth at which the local temperature exceeds the mean temperature above it by 0.2°C, (c.f. Lucas et al. 2019). We note, however, that our computed mixed layer depths are not very sensitive to the particular definition used; changing the specific criterion leads to average mixed layer depths within 2 m of the values shown here (Supplemental Material §1). As in the OWS Papa mooring data, the upper ocean structure stays relatively consistent for the first part of the season: the mixed layer deepens at an average rate of $0.2\,\mathrm{m\,day^{-1}}$ and its potential density stays at approximately $1024.1\,\mathrm{kg\,m^{-3}}$. After yearday 290, concurrent with the increase in winds and shift to surface cooling, the mixed layer deepens at a faster rate ($\sim 0.34\,\mathrm{m\,day^{-1}}$) and its density increases by approximately $0.5\,\mathrm{kg\,m^{-3}}$. In addition to the $\sim 20\,\mathrm{m}$ increase in mixed layer depth over the full deployment, there is substantial temporal variability of $\pm 5 - 10\,\mathrm{m}$ on timescales of a couple of days. This variability is slower than tidal (semidiurnal) or inertial motions (which have a 15.6-hour period at this latitude).

We next consider the OSBL shear and stratification. The stratification is described by the squared buoyancy frequency $N^2 = -g/\rho_0\,\mathrm{d}\rho/\mathrm{d}z$, where $\rho_0 = 1025\,\mathrm{kg\,m^{-3}}$ is a characteristic density of seawater and g is the gravitational acceleration. Fig. 4(a) shows N^2 corresponding to the density structure in Fig. 3(d) (where the data have been gridded with a 0.5 m-vertical resolution). Also plotted are the mixed layer depth and an estimate of the transition layer base, defined here as the shallowest depth below the mixed layer where $N^2 < 0.0001\,\mathrm{s^{-2}}$ (Dohan and Davis 2010), though we note that there are many possible definitions for the TL depth (Johnston and Rudnick 2009). Together, the estimated depths of the mixed layer base and transition layer base suggest TL thicknesses varying between approximately 10 m and 20 m throughout the deployment, consistent with the values observed by Johnston and Rudnick (2009).

From the definitions of the ML and TL bases, the transition layer is more strongly-stratified than either the mixed layer or pycnocline (Fig. 4a). The maximum stratification varies throughout the deployment – for example, N^2 weakens around yeardays 293-298, shortly after a sharp peak in wind stress and coincident with net surface cooling seen(Fig. 2). However, even with this time variation the transition layer remains strongly stratified, with $N^2 \sim O(10^{-3})\,\mathrm{s^{-2}}$ on vertical scales of 0.5 m throughout the entire deployment.

To calculate the vertical shear, $S^2 = (\mathrm{d}u/\mathrm{d}z)^2 + (\mathrm{d}v/\mathrm{d}z)^2$, we use an approach commonly applied to lowered ADCP measurements (Firing and Gordon 1990; Fischer and Visbeck 1993; Visbeck 2002). We calculate vertical shears from each individual LR ADCP ping while the float is profiling and then average the individual measurements in 0.5 m-bins. Because we seek the vertical shear and not the absolute velocity profile, we do not need to constrain the horizontal motion of the float itself during these measurements.

The resulting timeseries of S^2 is presented in Fig. 4(b). Note that there are gaps in the record around yeardays 270 and 280, as well as incomplete velocity profiles around yearday 300. We find that in addition to being strongly-stratified, the transition layer is also strongly-sheared: values of $S^2 \sim O(10^{-3})\,\mathrm{s}^{-2}$ are frequently observed for the 0.5 m vertical resolutions plotted here, particularly in the second half of the record. The shear is locally elevated in the transition layer compared with the lower mixed layer and the upper pycnocline. The vertical structures of shear and stratification are consistent with previous observations in this region (D'Asaro 1985b).

To further characterize the TL shear and stratification, in Fig. 5(a-b) we plot individual profiles of N^2 and S^2 referenced to the mixed layer depth. We also show the means $\overline{N^2}$ and $\overline{S^2}$ and standard deviations σ_{S^2} and σ_{N^2} of these depth-referenced profiles (calculated in 0.5 m-bins). The stratification exhibits a similar shape throughout the deployment, with a narrow peak of $O(10^{-3} - 10^{-2})\,\mathrm{s}^{-2}$ just below the ML base and weaker stratification in the deeper part of the transition layer and pycnocline; this vertical structure is reminiscent of TL observations in BBTRE and NATRE data (Sun et al. 2013). Profiles of the squared shear, on the other hand, suggest more variability (for example, $\sigma_{S^2}/\overline{S^2} \approx 100\%$ at the depth of $\overline{S^2}_{\mathrm{max}}$, compared with $\sigma_{N^2}/\overline{N^2} \approx 65\%$ at the depth of $\overline{N^2}_{\mathrm{max}}$) and broader peaks with respect to depth. This is in part due to the choice of reference depth: the location of the peak stratification is closely related to the mixed layer base, while peak values of shear may be slightly above or below this depth.

Comparing individual profiles of N^2 and S^2 suggests broader peaks in shear than stratification. To quantify this apparent difference, we follow Williamson et al. (2018) and define characteristic lengthscales describing the width of the velocity and density profiles as

$$\delta_b = -\frac{g}{\rho_0}\frac{\Delta\rho}{N^2_{\max}} \text{ and } \delta_s = \frac{\Delta U}{S_{\max}}, \tag{1}$$

where δ_b and δ_s are associated with the stratification and shear, respectively. The quantities $N^2_{\max}$ and $S_{\max} = \sqrt{S^2_{\max}}$ are the maximum buoyancy frequency and shear and $\Delta U = \Delta\sqrt{u^2+v^2}$ and $\Delta\rho$ are the overall differences in horizontal flow speed and density in the vicinity of the transition layer for individual profiles. Here, we compute these quantities between 10 m above and 20 m below the mixed layer base. The lengthscales δ_b and δ_s give a measure of how sharply-peaked the shear and stratification are; uniformly-sheared or -stratified profiles would have characteristic lengths of 30 m, while step changes in U or ρ would give lengthscales approaching zero.

Consistent with the timeseries data in Fig. 4(a,b) and the profiles in Fig. 5(a,b), both the shear and stratification vary over widths of approximately 5-10 m (Fig. 5c). δ_b and δ_s vary both in time and in relation to each other. For example, around yearday 290, the stratification is much sharper than the shear, while a few days later (following the peak in wind stress seen in Fig. 2a) the value of δ_b approaches that of δ_s. However, throughout the deployment, δ_s is almost always larger than δ_b: the shear is broader than the stratification.

Given the strong TL shear and stratification, it is natural to ask whether this region will be stable to shear instability. The Miles-Howard theorem states that an inviscid, steady, parallel, stably-stratified shear flow is linearly stable if the gradient Richardson number, $Ri_g = N^2/S^2$, is everywhere greater than 1/4 (Miles 1961; Howard 1961). While real oceanographic flows do not satisfy the assumptions behind the Miles-Howard theorem, Ri_g has nevertheless been used to characterize overall flow stability (e.g. Kunze et al. 1990; Large et al. 1994; Smyth and Moum 2013).

As an alternative to Ri_g, we consider the reduced shear $S^2 - 4N^2$, noting that $S^2 - 4N^2 > 0$ corresponds to $Ri_g < 1/4$. We plot the reduced shear based on the 0.5 m gridded stratification and bin-averaged shear in Fig. 4(c). It is important to recognize that when $|S^2 - 4N^2|$ is small, measurement noise may dominate the signal. We estimate the noise in our squared shear measurements in each depth bin following the approach in Fischer and Visbeck (1993) (Supplemental Material §3). Assuming that S^2 is the primary source of measurement error, we therefore note that when $|S^2 - 4N^2|$ is below this error threshold (light grey regions in Fig. 4c) we cannot say with certainty whether shear instability may be expected.

Outside of the transition layer, the reduced shear is small but positive (i.e. unstable) in the mixed layer and small but negative (i.e. stable) in the pycnocline, consistent with the weak shears in both regions and the stable stratification at depth. Within the transition layer, the overall magnitude of the reduced shear (whether positive or negative) is much larger, reflecting the stronger shear and stratification. The actual behaviour of the reduced shear throughout the deployment is quite complex. It is rare for the reduced shear to be positive across the majority of the transition layer (the main exception being yeardays 293-298 when the highest shears are observed). However, there are typically at least some depths within the transition layer with positive reduced shear throughout much of the deployment, suggesting the possibility of shear instability for the observed flows.

The reduced shear may be used to predict the turbulent kinetic energy (TKE) dissipation rate ε under the assumption of KH instability returning the reduced shear to zero. Using the parameterization of Kunze et al. (1990) for values of $|S^2 - 4N^2|$ above the error threshold, we predict average values of $\varepsilon = 1.1 \times 10^{-9}\,\mathrm{m^2\,s^{-3}}$ before yearday 290 and $2.1 \times 10^{-9}\,\mathrm{m^2\,s^{-3}}$ after. (Using a threshold of 0 changes these estimates by less than 5%.) These values are lower than other measurements of TL dissipation (e.g. Sun et al. 2013). We note, however, that the values plotted in Fig. 4 have a vertical resolution of 0.5 m; it is entirely possible that smaller Ri_g (larger $S^2 - 4N^2$) would be found at finer vertical resolutions (Smyth and Moum 2013). With this in mind, in the following subsection we present data from the thermistor chains in order to examine the TL flows in more detail.

b. High-resolution temperature features in the transition layer

As described in section 2 and shown schematically in Fig. 1(b), between successive profiles of the upper ocean the float drifted in Lagrangian mode at different depths in the transition layer, moving to a new level approximately once per hour. As a result, during the 73-day deployment the T-chains captured a variety of features with a vertical resolution of 6 cm and a temporal resolution of 1/3 Hz.

Fig. 6(a) shows approximately 8.5 hours of temperature structure associated with one such drift period in depth-time coordinates (i.e. an Eulerian frame of reference). The float depth varies by approximately 10 m on timescales ranging from a few minutes to a few hours, in addition to the hourly programmed float movements. Motions on these timescales are ubiquitous in the upper ocean due to ambient internal waves (Garrett and Munk 1979).

Representative examples of different temperature features are shown in the depth and float frames of reference in the bottom rows of Fig. 6, and in the float frame of reference in Fig. 7. Fig. 6(b,e) and 7(a) show what we interpret as the signature of an overturning turbulent mixing event: an initially stratified interface becomes highly energetic, leading to strong motions of the interface and a general broadening of the stratified layer, consistent with a KH-type shear instability (Smyth and Moum 2000; Mashayek et al. 2017). We note that formation of the classic KH billow may be disrupted by pre-existing turbulence (Kaminski and Smyth 2019), and as KH instability is stationary with respect to the mean flow, a Lagrangian observer moving with the flow may not see an initial overturn depending on its location in the developing shear instability (Supplemental

Material §5). As such, we argue that despite not seeing a billow-like structure, the temperature field in Fig. 7(a) is consistent with a KH-driven mixing event.

However, these KH-like events are rare in the T-chain measurements. More frequently observed, and perhaps more surprising, are the temperature structures shown in Fig. 6(d,g) and Fig. 7(b) and (c). The T-chain data reveal the frequent presence of very sharp temperature interfaces (Fig. 7b), with vertical variations of $\mathcal{O}(1°\mathrm{C})$ over distances of at most 6 cm (as indicated by the contours in Fig. 7), the vertical resolution of the T-chain. These interfaces are not only sharp but persistent, lasting for tens of minutes. The T-chain timeseries data also reveal the frequent presence of small strongly-stratified parcels of fluid adjacent to these sharp interfaces (Fig. 7c), with temperature differences of $\mathcal{O}(1°\mathrm{C})$ relative to their surroundings (recall that the thermistor resolution is 0.001°C). These temperature structures are typically $\lesssim \mathcal{O}(10)$ cm, appear to last for several minutes at a time, and have a temperature difference from their surroundings similar to that across the interface. They are seen in the two separate T-chain measures on opposite sides of the float, suggesting they are not artifacts indicative of a wake. These small features do not appear to smear out the interface; rather, the interface remains fairly sharp.

These interfaces do not always exist in isolation. Fig. 6(c,f) show the temperature structure as the float moves between successive depths in the transition layer (as indicated in Fig. 1b). There is clear evidence of interfaces at both depths (indicated by the dark-light red and light red-blue transitions; see also Supplemental Material §6). This suggests the existence at certain times of a "steppy" structure in TL temperature with $\mathcal{O}(1-2)$ m-thick layers. Similar steppy structures have been seen in other observations of the upper thermocline. For example, Moum (1996) observed turbulent thermocline patches with $\mathcal{O}(1\,\mathrm{m})$ layers and noted that transport was localized within individual layers with little fluid interaction across the distinct steps.

c. Quantification of temperature features

We can quantify the observed temperature structures using the Thorpe scale, L_T, which characterizes the size of overturns in a stratified fluid (Thorpe 1977). Given a density profile $\rho(z,t)$, L_T is defined as the root-mean-square average of the distance individual fluid parcels are moved, d, when adiabatically sorting the density into a statically-stable profile $\rho^\star$. That is,

$$L_T = \langle d^2 \rangle^{1/2}, \tag{2}$$

where angle brackets denote a vertical average.

The above definition includes the statically-stable portions of the initial profile ρ for which $d = 0$. This may bias the estimated lengthscale low when only a small section of a profile contains density inversions. Instead, it may be useful to consider only the statically-unstable portion of the profile (Moum 1996; Smyth et al. 2001; Diamessis and Nomura 2004). We therefore also define a conditional version of the Thorpe scale in which only non-zero parcel displacements are considered:

$$L'_T = \langle d^2 | d \neq 0 \rangle^{1/2}. \tag{3}$$

L_T and L'_T are related through the fraction of the profile that is statically unstable (Thorpe 1977).

The distributions of L_T and L'_T from the T-chain data during the float drift periods are presented in Fig. 8. The data are split into two time periods (yeardays 265-290 and 290-328), corresponding to the shift from relatively low winds and surface warming to increased winds and surface cooling (Fig. 2). As Fig. 8(a) shows, some sort of inversion is present in the majority of profiles throughout the deployment: L_T is nonzero approximately 85% of the time before yearday 290 and approximately 92% of the time after yearday 290. While Thorpe scales increase overall in the latter part of the deployment, the observed temperature structures are small throughout the deployment, with very few measurements of $L_T > 30$ cm. The small overturn sizes are particularly apparent in the distributions of L_T' (Fig. 8b): again, there are very few values larger than 30 cm (such as the event shown in Fig. 7a). In addition, a significant fraction of the observed temperature structures in the T-chain profiles are 6 cm or smaller (similar to the temperature features in Fig. 7c) – the minimum observable size for this vertical resolution.

d. Relating T-chain observations to mixed layer deepening

As seen in the previous section, the T-chain observations reveal a variety of small-scale features with very few large overturns. It is natural to ask whether these $O(10)$ cm features can be related to the observed large-scale ML deepening. That is, we would like to predict the rate at which the mixed layer would deepen based on the observed temperature structures, and compare to the overall OSBL evolution.

Let h denote the mixed layer depth, with $\mathrm{d}h/\mathrm{d}t$ representing mixed layer deepening (Price et al. 1978). Assuming lateral variability is negligible, we can model the change in ML depth as

$$\frac{\mathrm{d}h}{\mathrm{d}t} \approx w_e + \frac{\mathrm{d}z_{\rho_{ref}}}{\mathrm{d}t}, \tag{4}$$

where w_e is an entrainment velocity, i.e. the rate at which the ML base moves due to turbulent entrainment of the dense underlying fluid, and $z_{\rho_{ref}}$ is the depth of a reference isopycnal below the ML. The latter term represents large-scale heaving of the ML base by internal waves or eddies, which may lead to $O(10)$ m variations in mixed layer depth (Johnston and Rudnick 2009; Sun et al. 2013; Lucas et al. 2019). We represent this term using the depth of the $\rho = 1025.5\,\mathrm{kg\,m^{-3}}$ isopycnal (calculated from the twice-daily float profiles), chosen as it lies below the ML base during the deployment but not so far below as to be removed from the dynamics of the OSBL.

The entrainment velocity is defined as

$$w_e = \frac{\overline{\rho' w'}}{\Delta\rho} = \frac{\mathcal{B}}{g'}, \tag{5}$$

where $\mathcal{B}$ is an entrainment buoyancy flux, often written as $\mathcal{B} = g/\rho_0 \overline{\rho' w'}$ (where $g' = g\Delta\rho/\rho_0$ is the reduced gravity, calculated using the density difference from the CTD measurements) (Strang and Fernando 2001), but more precisely defined as the diapycnal flux of buoyancy due to mixing (Winters and D'Asaro 1996). Exact computation of this quantity requires more detailed information than is measured here and its estimation is an important problem in small-scale physical oceanograpy (Gregg 1987). Here, we use the observed inversions in the T-chain data to estimate $\mathcal{B}$.

As described above, the geometry of a given density inversion (which we assume to be well characterized by temperature in the transition layer, see appendix 6) can be estimated using L_T. However, there are a variety of other lengthscales which can be used to describe a turbulent stratified flow (Smyth and Moum 2000; Mashayek et al. 2017), and we can exploit the relationships between these lengthscales. In particular, here we focus on two additional lengthscales: the Ozmidov scale, L_O, and the Ellison scale, L_E.

The Ozmidov scale characterizes the largest overturns not affected by stratification and is defined as

$$L_O = \left(\frac{\varepsilon}{N^3}\right)^{1/2}, \tag{6}$$

where ε is the TKE dissipation rate and N is a characteristic stratification (discussed further below). Thermocline observations have shown that the Thorpe and Ozmidov scales are related, with an average ratio of $L_O/L_T \simeq 0.8$ (Dillon 1982). While this ratio may depend on the flow parameters (Taylor et al. 2019) and may vary in time for a given turbulent mixing event (Smyth and Moum 2000; Mashayek et al. 2017), here we use the observed ratio from Dillon (1982) and simply note that this choice carries with it some uncertainty. With this relationship between L_O and L_T, the

TKE dissipation rate can be estimated as

$$\varepsilon \simeq 0.64 L_T^2 N^3 \,. \tag{7}$$

Assuming a balance between production, dissipation, and buoyancy flux, i.e. assuming the turbulence is quasi-steady when appropriately averaged (Osborn 1980), $\mathcal{B}$ can then be parameterized as

$$\mathcal{B} = \Gamma\varepsilon \simeq 0.64 \Gamma L_T^2 N^3 \,. \tag{8}$$

While the turbulent flux coefficient Γ has been shown to depend on the flow parameters and the mixing mechanism (Gregg et al. 2018), here we use the standard assumption that $\Gamma \approx 0.2$. This L_T-based parameterization has been used in previous studies to interpret observational data (e.g. Mater et al. 2015; Smith 2020) and to model buoyancy fluxes in numerical simulations (e.g. Klymak and Legg 2010).

Equation (8) requires a characteristic stratification, N, representing the background stratification against which turbulence is working. The "correct" choice of N is a key question in studies of stratified turbulence (Winters and D'Asaro 1996; Arthur et al. 2017). One option is to use a uniform stratification across the float, N_{float} (defined using the density difference and distance between the two CTDs). However, the T-chain data show that the stratification is highly nonuniform. To account for this, we estimate a characteristic "bulk" stratification dynamically relevant to the overturning features using the Ellison scale L_E, which describes the energy-containing scales of a turbulent flow (Itsweire 1984; Smyth and Moum 2000). Following Smyth et al. (2001), we define

$$L_E = \frac{T'_{\text{rms}}}{T_{E,z}} = \frac{\langle (T - T^\star)^2 \rangle^{1/2}}{T_{E,z}}, \tag{9}$$

where $T_{E,z}$ is a characteristic bulk temperature gradient. We note that here we have defined T' using the sorted temperature profile $T^\star$, rather than a mean temperature profile $\overline{T}$. Defining a bulk stratification $N_E^2 \equiv \alpha g T_{E,z}$ (assuming that the stratification is primarily due to temperature, see appendix 6) and using $L_E \sim L_T$, we can calculate N_E as

$$N_E^2 = \alpha g \frac{\langle (T - T^\star) \rangle}{L_T} \,. \tag{10}$$

As discussed in Smyth et al. (2001), N_E^2 is essentially an overturn-weighted stratification and $N_E^2 L_T^2/2$ describes well the available potential energy of the overturns (appendix 6). We therefore use N_E in our estimate of the buoyancy flux, $\mathcal{B} \simeq 0.64 \Gamma L_T^2 N_E^3$. Substituting back into equation (5) allows us to estimate the entrainment velocity as

$$w_e \simeq \frac{0.64 \Gamma L_T^2 N_E^3}{g'} \,. \tag{11}$$

We note that the above expression uses the CTD and T-chain data only. Assuming that these local estimates of w_e are representative of the overall entrainment through the transition layer, we can model the anticipated change in mixed layer depth due to entrainment as

$$\Delta h_e(t) \simeq \int_0^t \frac{0.64 \Gamma L_T(t')^2 N_E(t')^3}{g'(t')} \, \mathrm{d}t' \,. \tag{12}$$

The changes in mixed layer depth associated with entrainment and heaving of the ML base can therefore be estimated and compared to the observed depths (Fig. 9). It is clear that while heaving of the mixed layer base may account for significant short-term changes in mixed layer depth, these changes do not lead to an overall deepening of the OSBL during the float deployment. On the other hand, the entrainment-based estimate accurately describes the observed change in mixed layer depth. This quantitative agreement is found in spite of the assumptions in the derivation of equation (12), such as neglecting lateral variability and assuming constant values for L_O/L_T and Γ. The combined effects of entrainment and heaving capture the overall evolution of the mixed layer depth well, both qualitatively and quantitatively. Altogether, Fig. 9 suggests that the frequent small-scale temperature structures seen in the T-chain data can indeed account for the observed deepening. That is, based on the observations presented here, mixed layer deepening is accomplished by persistent scouring motions at the base of the mixed layer rather than larger-scale isolated overturning events.

e. Fluxes and diffusivity

From the previous section, it is clear that turbulent mixing and entrainment at the ML base depend on both individual overturn size and stratification. We have already seen that the majority of observed overturns are $\lesssim 30\,\mathrm{cm}$ in size (Fig. 8). In Fig. 10(a), we further characterize the temperature structures in terms of N_E^2. From the distributions of L_T and N_E^2, it is clear that, in addition to occurring less frequently, the largest overturns are typically associated with weaker $N_E^2 \sim 10^{-4}\,\mathrm{s}^{-2}$. Smaller overturns exhibit a wider range of N_E^2 values, peaking around $10^{-4} - 10^{-3}\,\mathrm{s}^{-2}$.

The solid lines in Fig. 10(b) show the probability density functions of ε estimated using (7) (where the area under the curve between two values gives the probability of ε falling between those values). The corresponding medians and means are also indicated on the Fig. and listed in table 1. The estimated dissipation rates span several orders of magnitude, increase in the latter part of the deployment, and are strongly skewed towards lower values: medians are $O(10^{-8})\,\mathrm{m}^2\,\mathrm{s}^{-3}$ and means are approximately six times larger. These values are consistent with estimated TL dissipation rates in NATRE and BBTRE data (Sun et al. 2013).

While high-ε events are relatively infrequent, they can contribute significantly to the overall flux across the ML base. To show this, we consider the distributions of ε weighted by their contribution towards the net dissipation over the entire deployment following D'Asaro (1985a) (dotted lines in Fig. 10b). The area under this distribution is proportional to the average ϵ. From these distributions, it is clear that the data is sufficient to compute the average since the area is well-defined and that events with $\varepsilon \sim O(10^{-8} - 10^{-7})\,\mathrm{m}^2\,\mathrm{s}^{-3}$ account for the majority of the TL dissipation. These values of ε are larger than the predictions based on the Kunze et al. (1990) reduced shear parameterization (section a), further underlining the importance of including these small-scale temperature features in estimates of transition layer turbulence.

The distributions of ε are quasi-lognormal (although skewed towards smaller values, see Supplemental Material §7), consistent with an intermittent turbulent flow. Assuming a lognormal distribution, the degree of intermittency in ε can be quantified by the "intermittency factor" $\sigma^2_{\ln\varepsilon}$ (Baker and Gibson 1987). For the observations presented here, we find intermittency factors of 2.01 and 1.90 for the early and late parts of the deployment, respectively. These values are similar to intermittency factors found in the pycnocline (e.g. Wijisekera et al. 1993; Lozovatsky et al. 2017), although not so high as to suggest that the flow is dominated by large-scale lateral stirring (Baker and Gibson 1987).

In addition to ε, mixing is often quantified by a scalar diffusivity,

$$K_z = \frac{g}{\rho_0}\frac{\overline{\rho' w'}}{N^2} = \frac{\mathcal{B}}{N^2}\,. \tag{13}$$

As with other stratified turbulent quantities, the diffusivity depends on the particular choice of N (Winters and D'Asaro 1996; Arthur et al. 2017). Here, we consider two versions of K_z,

$$K_E \equiv \frac{\mathcal{B}}{N_E^2} \approx 0.64\Gamma L_T^2 N_E\,,\; K_{\mathrm{float}} \equiv \frac{\mathcal{B}}{N_{\mathrm{float}}^2} \approx \frac{0.64\Gamma L_T^2 N_E^3}{N_{\mathrm{float}}^2}\,. \tag{14}$$

In the above, K_E corresponds to a diffusivity associated with the individual small-scale temperature features (and hence uses the overturn-weighted stratification N_E) while K_{float} uses the average stratification across the float, representing a diffusivity on $O(2)$ m-scales.

As with ε, the computed diffusivities span several orders of magnitude (solid contours in Fig. 10a), with the highest values typically corresponding to the largest overturns. The mean values of both K_E and K_{float} are larger than their respective median values by factors of approximately two and five, respectively (table 1), consistent with an intermittent turbulent flow. We also note that the average diffusivity depends on the particular choice of stratification used in (14): the mean and median values of K_{float} are smaller than those for K_E, consistent with $N^2_{\mathrm{float}} > N^2_E$ in most cases (appendix 6) and suggesting a strong dependence on the particular vertical scales over which motions are resolved.

f. Mixed layer heat budget

In section d, we showed that the small-scale features from the T-chain measurements can account for the overall ML deepening. These entrainment values may be further applied to estimate the overall heat flux through the ML base, and therefore the impact of transition layer mixing on upper ocean heat content. As before, we assume that lateral processes are weak (Pelland et al. 2016) and use a one-dimensional heat budget for mixed layer temperature in which mixed layer heat content is primarily controlled by surface fluxes and entrainment at the mixed layer base (Kraus and Turner 1967; Stephens et al. 2005). That is,

$$\rho_0 c_p h \frac{\mathrm{d}T_{\mathrm{ML}}}{\mathrm{d}t} \approx q_{\mathrm{net}} - q_{\mathrm{pen}} - q_{\mathrm{ent}}, \tag{15}$$

where T_{ML} is the average ML temperature, T_{TLB} is the temperature at the TL base, q_{pen} is the radiative heat flux penetrating through the ML base and c_p is the volumetric heat capacity of water. We take $\rho_0 c_p = 4.088 \times 10^6$ J/(°C m^3) and $q_{\mathrm{pen}} = 0.38 q_{\mathrm{sw}} \mathrm{e}^{-\lambda h}$, with q_{sw} the incident shortwave radiation and $\lambda = 20\,\mathrm{m}^{-1}$ (Cronin et al. 2015). We estimate the heat flux associated with transition layer entrainment using w_e (section d) and the temperature difference across the transition layer:

$$q_{\mathrm{ent}} = \rho_0 c_p w_e (T_{\mathrm{ML}} - T_{\mathrm{TLB}}) \tag{16}$$

where T_{TLB} is the temperature at the TL base.

Averaging the entrainment velocity and OWS Papa data over the drift periods between successive twice-daily OSBL profiles, we can thus calculate q_{ent}, $q_{\mathrm{net}} - q_{\mathrm{pen}}$, and the corresponding mixed layer temperature (Fig. 11). In the early part of the deployment $q_{\mathrm{ent}} \sim O(10-100)\,\mathrm{W\,m^{-2}}$, increasing to values $\sim O(100-300)\,\mathrm{W\,m^{-2}}$ in the later part. These q_{ent} values are consistent with fluxes computed at the ML base using OWS Papa data in previous studies (Cronin et al. 2015).

The predicted temperature evolution from equation (15) can be compared to the observed mixed layer temperature from the twice-daily large-scale float profiles (Fig. 11b). As with the predicted ML deepening (Fig. 9), the observed and predicted temperatures agree well both qualitatively (with small temperature changes in the early part and larger changes when fluxes increase later on) and quantitatively (differing by less than 0.5°C over the course of the deployment), despite the assumptions inherent in equation (15).

Together, the surface and entrainment heat fluxes and the evolution of T_{ML} suggest a fundamental shift in behaviour around yearday 290. Early in the deployment, the net surface heating and transition layer entrainment generally have similar magnitudes but opposite sign. As a result, they act in opposition, leading to little change in T_{ML}. However, with the shift to surface cooling and the increased entrainment after yearday 290, both fluxes act to cool the mixed layer and decrease T_{ML}. The role of the relative signs and magnitudes of the fluxes at the surface and ML base in controlling mixed layer temperature has been documented in previous studies; for example, the difference between entrainment and surface heating helps to regulate sea surface temperature in the equatorial Pacific cold tongue on seasonal (Moum et al. 2013) and ENSO timescales (Warner and Moum 2019).

4. Summary and discussion

Here we have presented observations of mixed layer deepening in the northeastern Pacific from a Lagrangian float in Fall 2018, as well as corresponding surface forcing and flux observations from nearby Ocean Weather Station Papa. The float-based measurements included twice-daily profiles over the upper ~ 120 m and Langrangian observations within the transition layer. Our observations can be summarized as follows:

- The mixed layer deepened by approximately 20 m during the deployment (from late September to early December), with corresponding transition layer thicknesses of 10-20 m. During this time, there was a shift from stabilizing to destabilizing surface heat fluxes and an overall increase in wind forcing.
- Strong shear and stratification ($N^2, S^2 \sim 0.001 - 0.01$ s^{-2}) were observed within the transition layer. The large-scale velocity profiles typically varied over a broader depth range than the corresponding density profiles.
- The T-chain observations showed a variety of temperature structures suggesting different mixing mechanisms. Infrequent KH-type overturning events were identified, broadening temperature interfaces when present. However, these were not the only structures observed. Sharp ($\Delta T \sim 1°$C over ~ 6 cm), long-lived temperature interfaces were observed, and were often accompanied by small, strongly-stratified temperature inversions adjacent to the interface, characteristic of scouring motions. In addition, these interfaces were not necessarily isolated, with suggestion of layered temperature stratifications on larger vertical scales.
- Most of the overturns were $O(10)$ cm or smaller in size, with temperature inversions present in the majority of T-chain profiles and slightly larger scales later in the study period.
- Using the observed overturn scales and an overturn-weighted stratification (Smyth et al. 2001), the entrainment velocity associated with these structures was estimated and found to agree well (with an rms error of less than 5 m) with the observed mixed layer deepening. The mixed layer temperature estimated using the corresponding transition layer heat flux in a one-dimensional upper ocean heat budget also agreed well with the observations (to within 0.5°C).

- The $O(10^{-6})\,\mathrm{m^2\,s^{-1}}$ average turbulent scalar diffusivities and $O(10^{-8})\,\mathrm{m^2\,s^{-3}}$ average dissipation rates estimated from the Thorpe scale analysis also agreed well with previous TL estimates (Sun et al. 2013).

Our observations suggest a "typical" transition layer mixing event during this deployment characterized by a $\sim 1°\mathrm{C}$ temperature difference, a $\sim 10\,\mathrm{cm}$-wide shear layer, and a $O(10^{-8})\,\mathrm{m^2\,s^{-3}}$ dissipation rate. Assuming a bulk Richardson number $Ri_b = -g\Delta\rho/\rho_0\Delta U^2 \sim O(1)$, we estimate a typical Reynolds number of $O(1000)$ characterizing the associated stratified shear flows. Similarly, using our estimates of ε and N_E^2, we find buoyancy Reynolds numbers $Re_b = \varepsilon/\nu N_E^2 \sim O(50-100)$. These Reynolds numbers are within the range of recent direct numerical simulation (DNS) studies of shear instabilities (e.g. Salehipour et al. 2016; Mashayek et al. 2017; Kaminski and Smyth 2019); as such, comparison with DNS may be a promising avenue for further analysis of the observed transition layer features. For example, simulations may be used to interrogate the assumptions made in the L_T-based analysis or to parameterize the fluxes in terms of larger-scale flow variables.

We have shown here that the observed TL temperature features can account for the overall changes in ML depth and temperature throughout the deployment. These small-scale features may be associated with a rich variety of dynamical processes (including shear instabilities, breaking internal waves, and interactions with ML turbulence). Indeed, the occurrence of both scouring and overturning features in the high-resolution temperature observations (Fig. 7) supports this idea. Ideally, we would like to definitively identify the specific waves and instabilities behind these features at various times and connect them to the $O(10)\,\mathrm{m}$ TL shear and stratification (Fig. 5) and the surface wind, wave, and buoyancy forcing. Insight into the underlying mechanisms may be gained, for example, by analyzing the linear stability of the observed profiles (as in Smyth et al. (2001)) and characterizing the computed modes (Carpenter et al. 2010; Eaves and Balmforth 2019), by using the ADCP measurements to describe the overlying ML turbulence, or by using the motion of the float itself to infer wave phase speeds within the TL. We note, however, that care must be taken when relating oceanographic observations with no true "initial condition" to the initial-value approach commonly employed in studies of fluid instabilities. Future work will need to focus on understanding the relationship between instantaneous or averaged flow profiles and the results of linear stability analysis in order to accurately interpret the measurements presented here.

To accurately parameterize OSBL evolution, it will be necessary to establish the relationship between the observed dissipation and entrainment and the surface and ML forcing. Indeed, predicting entrainment in terms of this forcing is a major goal of existing OSBL parameterizations (Li et al. 2019). In recent years, these have shown major advances, mostly by tuning their response to match large eddy simulation (LES) models. However, the small-scale temperature structures described here pose additional challenges for parameterizing TL mixing, illustrated, for example, by the sensitivity of K_z to the particular choice of stratification (section e): the diffusivities associated with individual temperature inversions (K_E) are much larger than those associated with the $O(2)$ m stratification (K_{float}). This strong dependence on the resolved vertical scale is not necessarily surprising, given that temperature structures seen here suggest scouring motions, which are *antidiffusive* in nature (Caulfield 2021). How to represent these physics in LES and TL models is therefore a key question. Future work will focus on using the estimated fluxes and entrainment data, along with forcing data from OWS Papa, to evaluate the impact of these unresolved structures on OSBL parameterizations.

The high-resolution observations presented here reveal a variety of different features acting on lengthscales down to a few centimeters and timescales of minutes. Despite their small scale, these features play an important role in driving the OSBL evolution. Incorporating these processes into future transition layer parameterization will allow for improved upper ocean models.

5. Acknowledgements

This work was supported by National Science Foundation grant OCE-1657676. We thank Roberta Hamme, the officers and crew of the John P. Tully and the Line-P team for deploying the float. This work was only possible due to the technical expertise and dedication of APL/UW staff.

6. Data availability statement

Surface forcing data from Ocean Weather Station Papa was provided by the NOAA/PMEL OCS Project Office (https://www.pmel.noaa.gov/ocs/). The TLF observations will be made available at the University of Washington ResearchWorks Archive.

APPENDIX A

Relationship between ρ and T in the transition layer

The bulk of our analysis relies on the assumption that the TL temperature field is representative of the density stratification, allowing us to use the T-chain measurements without salinity data. Here we consider the relationship between temperature and salinity in the CTD measurements to support this choice.

Fig. 6(a) shows the conservative temperature Θ and absolute salinity S_A computed from the CTD measurements (McDougall and Barker 2011) for the entirety of the float deployment, with darker colours denoting later dates. There is a clear shift in the $T-S$ relationship at lower temperatures, corresponding to measurements below the OSBL. This is consistent with the profiles in Fig. 3, which suggest stronger contributions of temperature to the stratification in the uppermost part of the water column and stronger salinity stratification at depth. While the $\Theta - S_A$ relationship varies in time, in general the temperature and salinity are well constrained for these observations.

To estimate the potential density from the T-chain measurements, we consider the measured CTD temperature T and corresponding potential density ρ during the Lagrangian drift periods. Fig. 6(b) shows a typical example of this relationship for one of the nine-hour drift periods between successive profiles. It is clear that ρ is well-described by a linear fit to T at these depths over this time period. As such, we use linear fits from the CTD measurements to estimate ρ for the T-chain measurements. We recalculate the fit for each individual drift period (between successive large-scale profiles) in order to accommodate the time dependence in the $\Theta - S_A$ relationship seen in panel (a).

APPENDIX B

Use of weighted stratification

The available potential energy (APE) describes the fraction of a flow's potential energy which is able to drive motion. For a one-dimensional profile, the APE can be defined as the difference in potential energy between the observed ρ and a profile $\rho^\star$ in which the potential density has been adiabatically resorted into a statically-stable configuration:

$$\mathrm{APE} = \int_z (\rho - \rho^\star) g z \, \mathrm{d}z \,. \tag{B1}$$

For a uniform background stratification $N = N_{\mathrm{const}}$, the APE can be related to the Thorpe scale as (Dillon 1982; Dillon and Park 1987)

$$\mathrm{APE} \simeq \frac{1}{2} N_{\mathrm{const}}^2 L_T^2 , \tag{B2}$$

while this approximation breaks down in cases where $\rho^\star$ varies rapidly in the vertical (Scotti 2015).

However, a uniform stratification is not an appropriate approximation in many of the TL observations presented above (particularly cases with sharp temperature interfaces). Instead, in section d we use an overturn-weighted stratification N_E, derived by assuming that $L_T \sim L_E$. We compare this weighted stratification to a linear fit to the potential density measured by the CTDs in Fig. 6(a). While there is considerable scatter, in general $N_E^2 < N_{\mathrm{float}}^2$, consistent with overturns occurring in a relatively weak stratification adjacent to a locally-stronger stratification (Fig. 6 and 7).

We can compare the APE calculated directly from equation (B1) to that estimated from L_T and either N_{float} or N_E (Fig. 6b). It is clear that the weighted stratification better describes the APE from the individual T-chain profiles across the range of observed overturns. This agreement further supports our choice of N_E as a characteristic stratification in the analysis of section d. We also note that the good agreement between the APE calculated directly and from (B2) suggests that N_E is similar to the "equivalent buoyancy frequency" suggested by Smith (2020).

References

Agrawal, Y. C., E. A. Terray, M. A. Donelan, P. A. Hwang, A. J. Williams III, W. M. Drennan, K. K. Khama, and S. A. Kitaigorodskii, 1992: Enhanced dissipation of kinetic energy beneath surface waves. *Nature*, **359**, 219–220.

Archer, D., 1995: Upper ocean physics as relevant to ecosystem dynamics: a tutorial. *Ecol. Appl.*, **5 (3)**, 724–739.

Arthur, R. S., S. K. Venayagamoorthy, J. R. Koseff, and O. B. Fringer, 2017: How we compute N matters to estimates of mixing in stratified flows. *J. Fluid Mech.*, **831**, R2.

Baker, M. A., and C. H. Gibson, 1987: Sampling turbulence in the stratified ocean: statistical consequences of strong intermittency. *J. Phys. Oceanogr.*, **17**, 1817–1836.

Belcher, S. E., and Coauthors, 2012: A global perspective of Langmuir turbulence in the ocean surface boundary layer. *Geophys. Res. Lett.*, **39**, L18 605.

Carpenter, J. R., N. J. Balmforth, and G. A. Lawrence, 2010: Identifying unstable modes in stratified shear layer. *Phys. Fluids*, **22**, 054 104.

Carpenter, J. R., G. A. Lawrence, and W. D. Smyth, 2007: Evolution and mixing of asymmetric Holmboe instabilities. *J. Fluid Mech.*, **582**, 103–132.

Caulfield, C. P., 2021: Layering, instabilities, and mixing in turbulent stratified flows. *Annu. Rev. Fluid Mech.*, **53**, 113–145.

Craik, A. D. D., and S. Leibovich, 1976: A rational model for Langmuir circulations. *J. Fluid Mech.*, **73 (3)**, 401–426.

Cronin, M. F., C. W. Fairall, and M. J. McPhaden, 2006: An assessment of buoy-derived and numerical weather prediction surface heat fluxes in the tropical Pacific. *J. Geophys. Res.*, **111**, C06 038.

Cronin, M. F., N. A. Pelland, S. R. Emerson, and W. R. Crawford, 2015: Estimating diffusivity from the mixed layer heat and salt balances in the North Pacific. *J. Geophys. Res. Oceans*, **120**, 7346–7362.

D'Asaro, E., 2018: Oceanographic floats: principles of operation. *Observing the Oceans in Real Time*, R. Venkatesan, A. Tandon, E. D'Asaro, and M. Atmanand, Eds., Springer Oceanography, Springer, Cham.

D'Asaro, E. A., 1985a: The energy flux from the wind to near-inertial motions in the surface mixed layer. *J. Phys. Oceanogr.*, **15**, 1043–1059.

D'Asaro, E. A., 1985b: Upper ocean temperature structure, inertial currents, and Richardson numbers observed during strong meteorological forcing. *J. Phys. Oceanogr.*, **15**, 943–962.

D'Asaro, E. A., 2003: Performance of autonomous Lagrangian floats. *J. Atmos. Oceanic Technol.*, **20**, 896–911.

D'Asaro, E. A., 2014: Turbulence in the upper-ocean mixed layer. *Annu. Rev. Mar. Sci.*, **6**, 101–115.

Deardorff, J. W., 1970: Convective velocity and temperature scales for the unstable planetary boundary layer and for Rayleigh convection. *J. Atmos. Sci.*, **27**, 1211–1213.

Diamessis, P. J., and K. K. Nomura, 2004: The structure and dynamics of overturns in stably stratified homogeneous turbulence. *J. Fluid Mech.*, **499**, 197–229.

Dillon, T. M., 1982: Vertical overturns: a comparison of Thorpe and Ozmidov length scales. *J. Geophys. Res.*, **87 (C12)**, 9601–9613.

Dillon, T. M., and M. M. Park, 1987: The available potential energy of overturns as an indicator of mixing in the seasonal thermocline. *J. Geophys. Res.*, **92 (C5)**, 5345–5353.

Dohan, K., and R. E. Davis, 2010: Mixing in the transition layer during two storm events. *J. Phys. Oceanogr.*, **41**, 42–66.

Eaves, T. S., and N. J. Balmforth, 2019: Instability of sheared density interfaces. *J. Fluid Mech.*, **860**, 145–171.

Fairall, C. W., E. F. Bradley, J. E. Hare, A. A. Grachev, and J. B. Edson, 2003: Bulk parameterization of air-sea fluxes: updates and verification for the COARE algorithm. *J. Climate*, **16**, 571–589.

Fernando, H. J. S., 1991: Turbulent mixing in stratified fluids. *Annu. Rev. Fluid Mech.*, **23**, 455–493.

Ferrari, R., and G. Boccaletti, 2004: Eddy-mixed layer interactions in the ocean. *Oceanography*, **17 (3)**, 12–21.

Firing, E., and R. L. Gordon, 1990: Deep ocean acoustic Doppler current profiling. *Proc. IEE Fourth Working Conf. on Current Measurements*, Clinton, MD, IEEE, 192-201.

Fischer, J., and M. Visbeck, 1993: Deep velocity profiling with self-contained ADCPs. *J. Atmos. Oceanic Technol.*, **10**, 764–773.

Gargett, A. E., T. B. Sanford, and T. R. Osborn, 1979: Surface mixing layers in the Sargasso Sea. *J. Phys. Oceanogr.*, **9**, 1090–1111.

Garrett, C., and W. Munk, 1979: Internal waves in the ocean. *Annu. Rev. Fluid Mech.*, **11**, 339–369.

Gregg, M. C., 1987: Diapycnal mixing in the thermocline: a review. *J. Geophys. Res.*, **92 (C5)**, 5249–5286.

Gregg, M. C., E. A. D'Asaro, J. J. Riley, and E. Kunze, 2018: Mixing efficiency in the ocean. *Annu. Rev. Mar. Sci.*, **10**, 443–473.

Hannoun, I. A., and E. J. List, 1988: Turbulent mixing at a shear-free density interface. *J. Fluid Mech.*, **189**, 211–234.

Harcourt, R. R., E. L. Steffen, R. W. Garwood, and E. A. D'Asaro, 2002: Fully Lagrangian floats in Labrador Sea deep convection: comparison of numerical and experimental results. *J. Phys. Oceanogr.*, **32**, 493–510.

Howard, L. N., 1961: Note on a paper of John W. Miles. *J. Fluid Mech.*, **10**, 509–512.

Huang, C. J., F. Qiao, and D. Dai, 2014: Evaluating CMIP5 simulations of mixed layer depth during summer. *J. Geophys. Res. Oceans*, **119**, 2568–2582.

Itsweire, E. C., 1984: Measurements of vertical overturns in a stably stratified turbulent flow. *Phys. Fluids*, **27 (4)**, 764–766.

Johnston, T. M. S., and D. L. Rudnick, 2009: Observations of the transition layer. *J. Phys. Oceanogr.*, **39**, 780–797.

Kaminski, A. K., and W. D. Smyth, 2019: Stratified shear instability in a field of pre-existing turbulence. *J. Fluid Mech.*, **862**, 639–658.

Klymak, J. M., and S. M. Legg, 2010: A simple mixing scheme for models that resolve breaking internal waves. *Ocean Model.*, **33**, 224–234.

Kraus, E. B., and J. S. Turner, 1967: A one-dimensional model of the season thermocline II. the general theory and its consequences. *Tellus*, **19 (1)**, 98–106.

Kukulka, T., A. J. Plueddemann, J. H. Trowbridge, and P. P. Sullivan, 2010: Rapid mixed layer deepening by the combination of Langmuir and shear instabilities: a case study. *J. Phys. Oceanogr.*, **40**, 2381–2400.

Kunze, E., A. J. Williams III, and M. G. Briscoe, 1990: Observations of shear and stability from a neutrally buoyant float. *J. Geophys. Res.*, **95 (C10)**, 18 127–18 142.

Large, W. G., J. C. McWilliams, and S. C. Doney, 1994: Oceanic vertical mixing: a review and a model with a nonlocal boundary layer parameterization. *Rev. Geophys.*, **32 (4)**, 363–403.

Li, M., P. G. Myers, and H. Freeland, 2005: An examination of historical mixed layer depths along Line P in the Gulf of Alaska. *Geophys. Res. Lett.*, **32**, L05 613.

Li, Q., and Coauthors, 2019: Comparing ocean surface boundary vertical mixing schemes including Langmuir turbulence. *J. Adv. Model. Earth Sys.*, **11**, 3545–3592.

Lozovatsky, I., H. J. S. Fernando, J. Planella-Morato, Z. Liu, J. H. Lee, and S. U. P. Jinadasa, 2017: Probability distribution of turbulent kinetic energy dissipation rate in ocean: observations and approximations. *J. Geophys. Res. Oceans*, **122**, 8293–8308.

Lucas, N. S., A. L. M. Grant, T. R. Rippeth, J. A. Polton, M. R. Palmer, L. Brannigan, and S. E. Belcher, 2019: Evolution of oceanic near-surface stratification in response to an autumn storm. *J. Phys. Oceanogr.*, **49**, 2961–2978.

Mahadevan, A., 2016: The impact of submesoscale physics on primary productivity of plankton. *Annu. Rev. Mar. Sci.*, **8**, 161–184.

Mashayek, A., C. P. Caulfield, and W. R. Peltier, 2017: Role of overturns in optimal mixing in stratified mixing layers. *J. Fluid Mech.*, **826**, 522–552.

Mater, B. D., S. K. Venayagamoorthy, L. St. Laurent, and J. N. Moum, 2015: Biases in Thorpe-scale estimates of turbulence dissipation. Part I: Assessments from large-scale overturns in oceanographic data. *J. Phys. Oceanogr.*, 2497–2521.

McDougall, T. J., and P. M. Barker, 2011: *Getting started with TEOS-10 and the Gibbs Seawater (GSW) Oceanographic Toolbox*. SCOR/IAPSO WG127, iSBN 978-0-646-55621-5.

Miles, J. W., 1961: On the stability of heterogeneous shear flows. *J. Fluid Mech.*, **10**, 496–508.

Moum, J. N., 1996: Efficiency of mixing in the main thermocline. *J. Geophys. Res.*, **101 (C5)**, 12 057–12 069.

Moum, J. N., A. Perlin, J. D. Nash, and M. J. McPhaden, 2013: Seasonal sea surface cooling in the equatorial Pacific cold tongue controlled by ocean mixing. *Nature*, **500**, 64–67.

Niiler, P. P., 1975: Deepening of the wind-mixed layer. *J. Mar. Res.*, **33 (3)**, 405–422.

Osborn, T. R., 1980: Estimates of the local rate of vertical diffusion from dissipation measurements. *J. Phys. Oceanogr.*, **10**, 83–89.

Pelland, N. A., C. C. Eriksen, and M. F. Cronin, 2016: Seaglider surveys at Ocean Station Papa: circulation and water mass properties in a meander of the North Pacific Current. *J. Geophys. Res. Oceans*, **121**, 6816–6846.

Price, J. F., 1979: On the scaling of stress-driven entrainment experiments. *J. Fluid Mech.*, **90 (3)**, 509–529.

Price, J. F., C. N. K. Mooers, and J. C. Van Leer, 1978: Observation and simulation of storm-induced mixed-layer deepening. *J. Phys. Oceanogr.*, **8**, 582–599.

Salehipour, H., C. P. Caulfield, and W. R. Peltier, 2016: Turbulent mixing due to the Holmboe wave instability at high Reynolds number. *J. Fluid Mech.*, **803**, 591–621.

Scotti, A., 2015: Biases in Thorpe-scale estimates of turbulent dissipation. part II: energetics arguments and turbulence simulations. *J. Phys. Oceanogr.*, **45**, 2522–2543.

Shcherbina, A. Y., E. A. D'Asaro, and S. Nylund, 2018: Observing finescale oceanic velocity structure with an autonomous Nortek acoustic Doppler current profiler. *J. Atmos. Oceanic Technol.*, **35**, 411–427.

Smith, J. A., 2020: A comparison of two methods using Thorpe sorting to estimate mixing. *J. Atmos. Oceanic Technol.*, **37**, 3–15.

Smith, K. M., C. P. Caulfield, and J. R. Taylor, 2021: Turbulence in forced stratified shear flows. *J. Fluid Mech.*, **910**, A42.

Smyth, W. D., and J. N. Moum, 2000: Length scales of turbulence in stably stratified mixing layers. *Phys. Fluids*, **12 (6)**, 1327–1342.

Smyth, W. D., and J. N. Moum, 2013: Marginal instability and deep cycle turbulence in the eastern equatorial Pacific Ocean. *Geophys. Res. Lett.*, **40**, 6181–6185.

Smyth, W. D., J. N. Moum, and D. R. Caldwell, 2001: The efficiency of mixing in turbulent patches: inferences from direct simulations and microstructure observations. *J. Phys. Oceanogr.*, **31**, 1969–1992.

Stephens, M. Y., R. J. Oglesby, and M. Maxey, 2005: A one-dimensional mixed layer ocean model for use in three-dimensional climate simulations: control simulation compared to observations. *J. Climate*, **18**, 2199–2221.

Strang, E. J., and H. J. S. Fernando, 2001: Entrainment and mixing in stratified shear flows. *J. Fluid Mech.*, **428**, 349–386.

Sun, O. M., S. R. Jayne, K. L. Polzin, B. A. Rahter, and L. C. St. Laurent, 2013: Scaling turbulent dissipation in the transition layer. *J. Phys. Oceanogr.*, **43**, 2475–2489.

Taylor, J. R., S. M. de Bruyn Kops, C. P. Caulfield, and P. F. Linden, 2019: Testing the assumptions underlying ocean mixing methodologies using direct numerical simulations. *J. Phys. Oceanogr.*, **49**, 2761–2779.

Thorpe, S. A., 1977: Turbulence and mixing in a Scottish Loch. *Philos. Trans. R. Soc. London Ser. A*, **286 (1334)**, 125–181.

van Haren, H., and L. Gostiaux, 2010: A deep-ocean Kelvin-Helmholtz billow train. *Geophys. Res. Lett.*, **37**, L03 605.

van Haren, H., L. Gostiaux, E. Morozov, and R. Tarakanov, 2014: Extremely long Kelvin-Helmholtz billow trains in the Romanche Fracture Zone. *Geophys. Res. Lett.*, **41**, 8445–8451.

Visbeck, M., 2002: Deep velocity profiling using lowered acoustic Doppler current profilers: bottom track and inverse solutions. *J. Atmos. Oceanic Technol.*, **19**, 794–807.

Warner, S. J., and J. N. Moum, 2019: Feedback of mixing to ENSO phase change. *Geophys. Res. Lett.*, **43**, 13 920–13 927.

Wijisekera, H. W., T. M. Dillon, and L. Padman, 1993: Some statistical and dynamical properties of turbulence in the oceanic pycnocline. *J. Geophys. Res.*, **98 (C12)**, 22 665–22 679.

Williamson, N., M. P. Kirkpatrick, and S. W. Armfield, 2018: Entrainment across a sheared density interface in a cavity flow. *J. Fluid Mech.*, **835**, 999–1021.

Winters, K. B., and E. A. D'Asaro, 1996: Diascalar flux and the rate of fluid mixing. *J. Fluid Mech.*, **317**, 179–193.

Woods, A. W., C. P. Caulfield, J. R. Landel, and A. Kuesters, 2010: Non-invasive turbulent mixing across a density interface in a turbulent Taylor-Couette flow. *J. Fluid Mech.*, **663**, 347–357.

Zhou, Q., J. R. Taylor, C. P. Caulfield, and P. F. Linden, 2017: Diapycnal mixing in layered stratified plane Couette flow quantified in a tracer-based coordinate. *J. Fluid Mech.*, **823**, 198–229.

LIST OF TABLES

TABLE 1. Mean and median TKE dissipation rates and diffusivities based on N_E and N_{float}, for the early part (before yearday 290), late part (after yearday 290), and full deployment.

	ε (m^2 s^{-3})	K_E (m^2 s^{-1})	K_{float} (m^2 s^{-1})
mean (early)	3.5×10^{-8}	8.5×10^{-6}	3.9×10^{-6}
median (early)	5.8×10^{-9}	3.6×10^{-6}	6.5×10^{-7}
mean (late)	5.9×10^{-8}	1.4×10^{-5}	8.6×10^{-6}
median (late)	1.1×10^{-8}	6.9×10^{-6}	1.7×10^{-6}
mean (full)	4.9×10^{-8}	1.2×10^{-5}	6.7×10^{-6}
median (full)	8.4×10^{-9}	5.3×10^{-6}	1.1×10^{-6}

LIST OF FIGURES

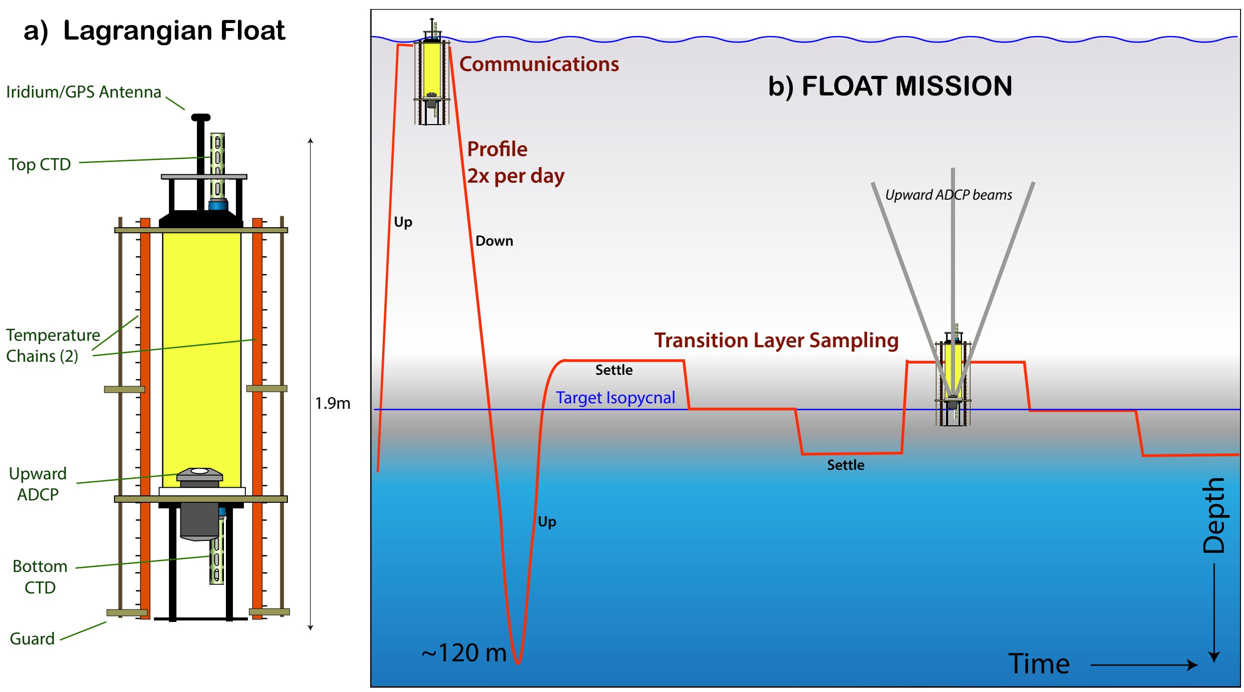

FIG. 1. (a) The Transition Layer Float. The float controls its buoyancy based on pressure, time and data from CTDs on the top and bottom. Thermistor chains on either side of the float body and an uplooking ADCP measure temperature and velocity profiles (b) Schematic representation of the float behaviour. The float surfaces for communications twice a day, profiling from the surface to about 120m. The transition layer isopycnal is chosen as 0.17 $\mathrm{kg\,m^{-3}}$ denser than the mixed layer density. The float seeks this isopycnal and then straddles it for 4000 s, then steps across the transition layer in 0.1 $\mathrm{kg\,m^{-3}}$ steps, seeking and straddling the isopycnal each time until it is time to surface.

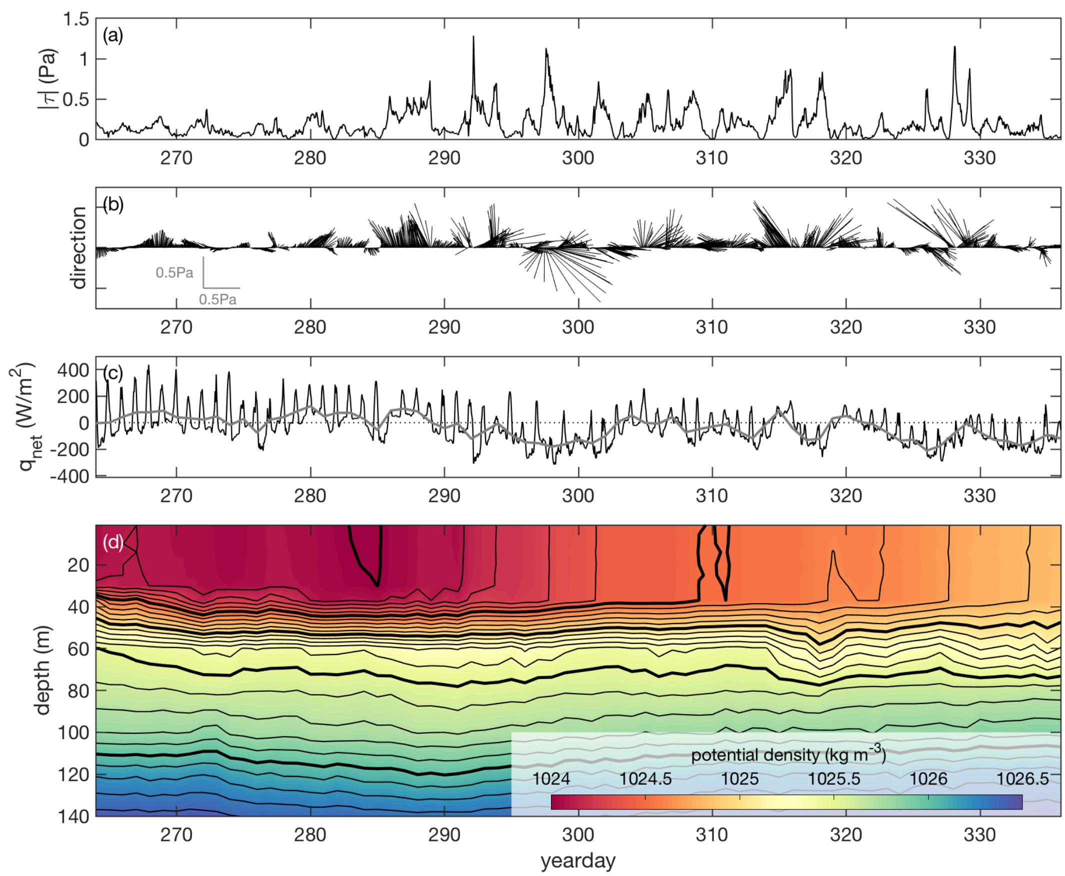

FIG. 2. Wind stress, net heat flux, and potential density data from OWS Papa during period of float deployment. (a,b) Wind stress magnitude $|\boldsymbol{\tau}|$ and direction (hourly). (c) Net surface heating, q_{net}, with hourly values plotted in black and daily averages plotted in grey. (d) Upper ocean potential density structure (daily average). Thick contour interval is $0.5\,\mathrm{kg\,m^{-3}}$ and thin contour interval is $0.1\,\mathrm{kg\,m^{-3}}$.

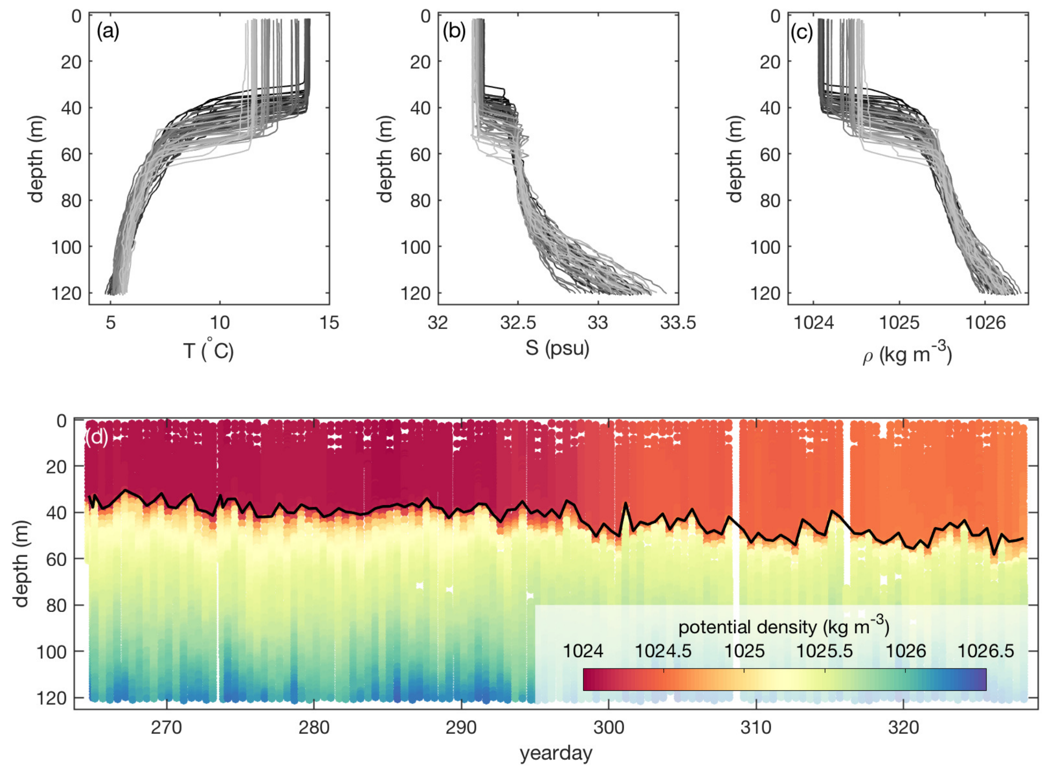

FIG. 3. Individual profiles of (a) temperature, (b) salinity, and (c) potential density obtained from the float CTDs in profiling mode. For clarity, every second profile is plotted. Lighter line colours correspond to profiles later in the deployment. (d) Upper ocean potential density structure from float profiles throughout entire deployment. The mixed layer depth is indicated by the solid black line.

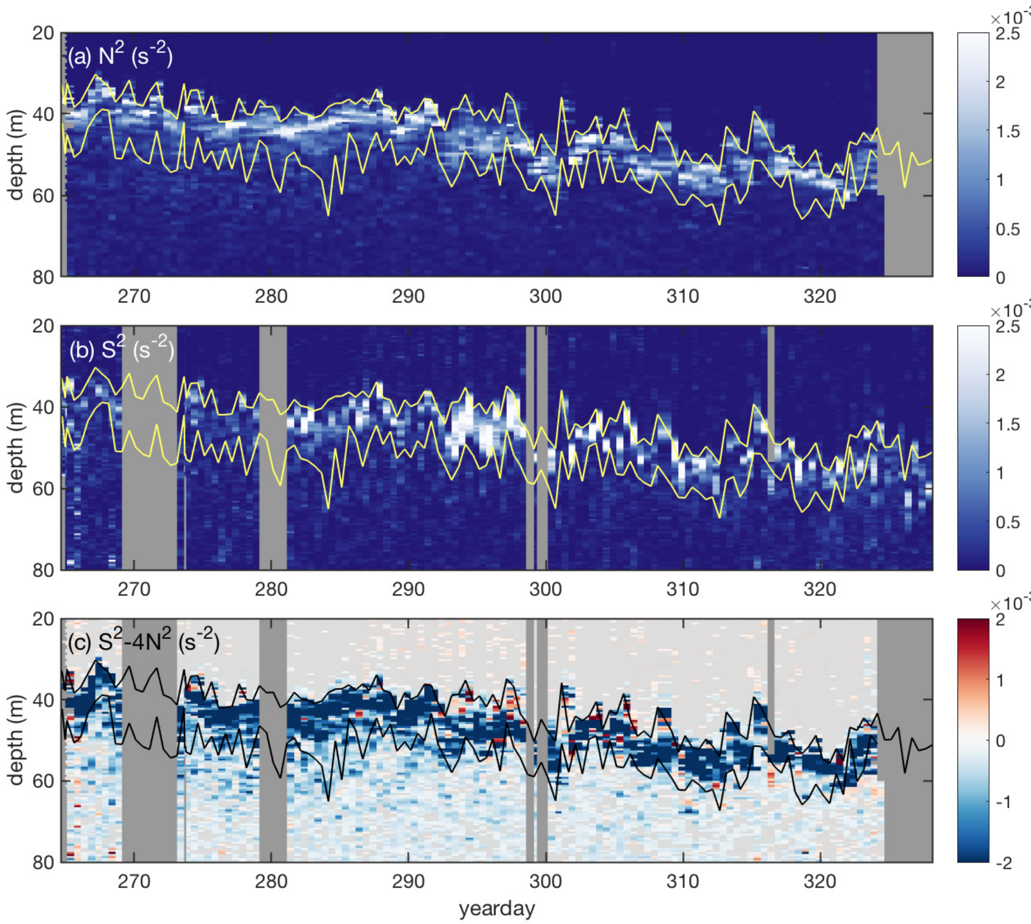

Fig. 4. (a) Buoyancy frequency, $N^2 = -g/\rho_0\, \mathrm{d}\rho/\mathrm{d}z$, calculated from CTD measurements and gridded. (b) Squared vertical shear, $S^2 = (\mathrm{d}u/\mathrm{d}z)^2 + (\mathrm{d}v/\mathrm{d}z)^2$, bin-averaged from LR ADCP measurements during float profiles. (c) Reduced shear, $S^2 - 4N^2$. Note that 0.5 m bins have been used to computed N^2 and S^2 here. The thin yellow/black lines correspond to the mixed layer depth (shallower) and transition layer base (deeper) computed based on the CTD data from the float profiles. The darker grey regions denote times or depths where no data were available, and the lighter grey regions in panel (c) denote locations where the magnitude of the squared shear is below the estimated error in shear.

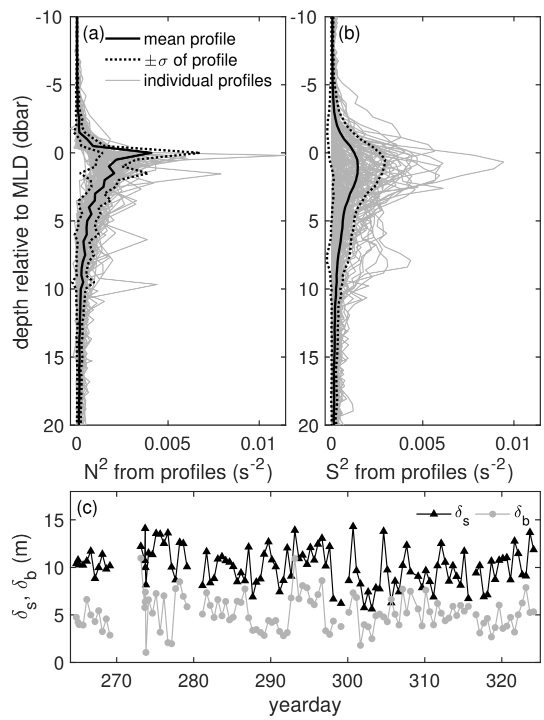

Fig. 5. Mean and individual profiles of (a) N^2 and (b) S^2, referenced to the mixed layer depth. Individual profiles are plotted with thin grey lines, mean profiles with thick black lines, and means ± one standard deviation with dotted black lines. (c) Characteristic lengthscales δ_s and δ_b of the shear and stratification, respectively, estimated from equation (1). The profiles shown here have a vertical resolution of 0.5 m.

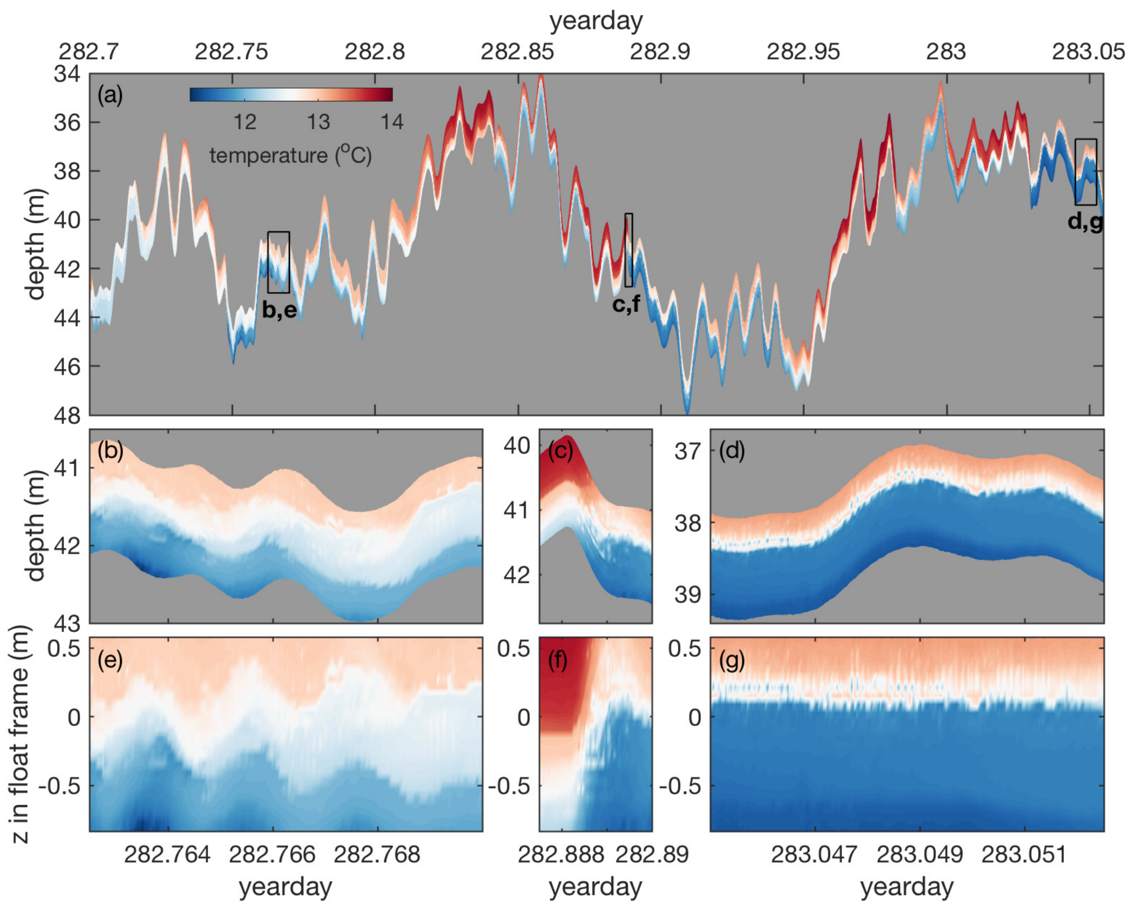

FIG. 6. (a) T-chain measurements of temperature structure in depth and time from one 8.5-hour period on yearday 282-283. (b)-(d) Close-up timeseries of temperature structure at three time periods as indicated by the boxes in (a), shown in both depth-time (middle row) and float (bottom row) frames of reference. (b,e) An overturning event. (c,f) Layered structure seen when the float moves to a new depth. (d,g) A scouring event. The temperature data shown here have a vertical resolution of 6 cm and a time resolution of 3 s.

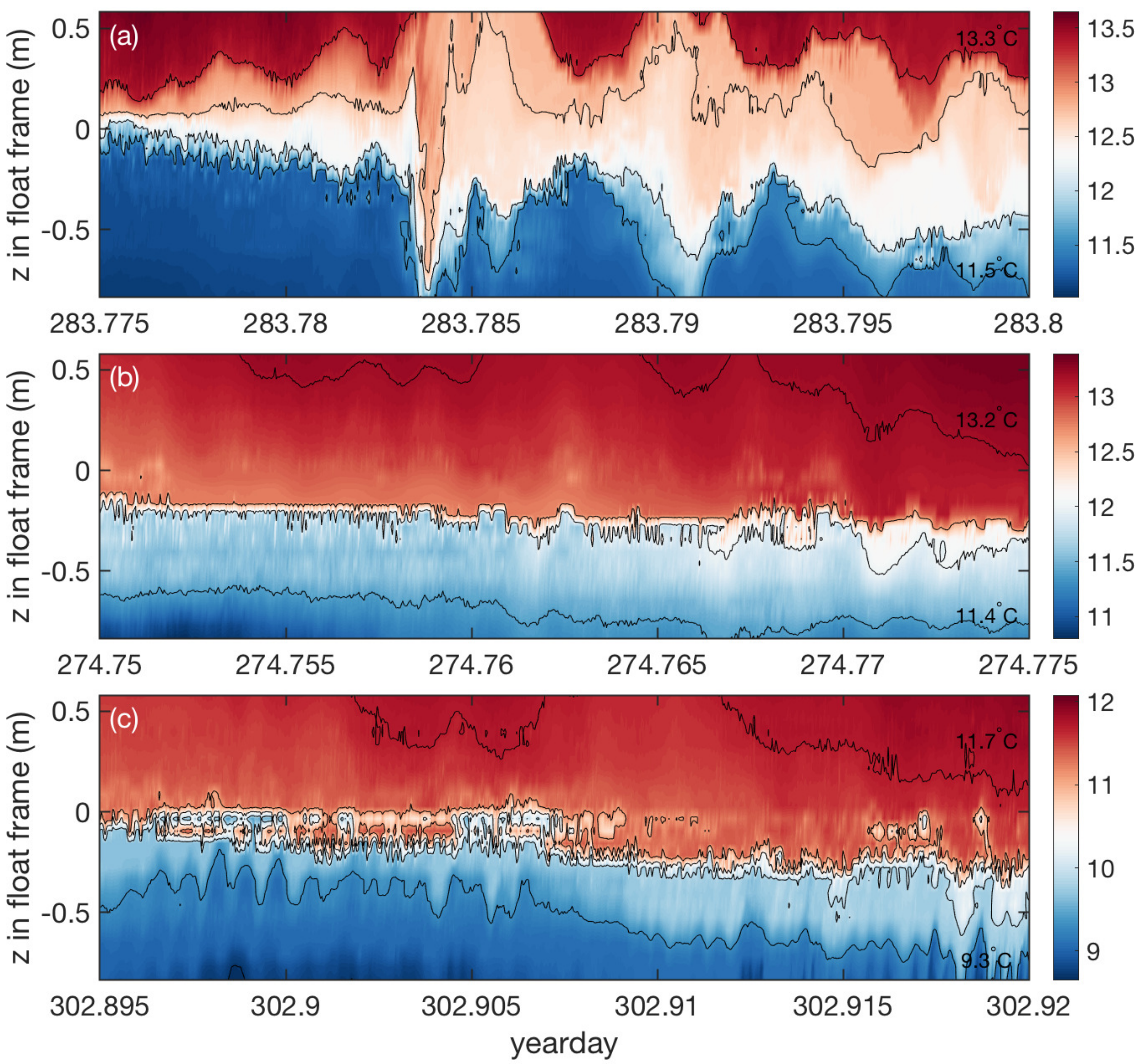

Fig. 7. Examples of different types of features in T-chain timeseries data. Each panel shows 36 min of data in the float frame of reference, and individual isotherms are contoured to highlight features. (a) Signature of a mixing event. (b) Sharp temperature interface. (c) Small, strongly-stratified overturns near an interface. The contour interval is 0.6°C. These data have a vertical resolution of 6 cm and a time resolution of 3 s.

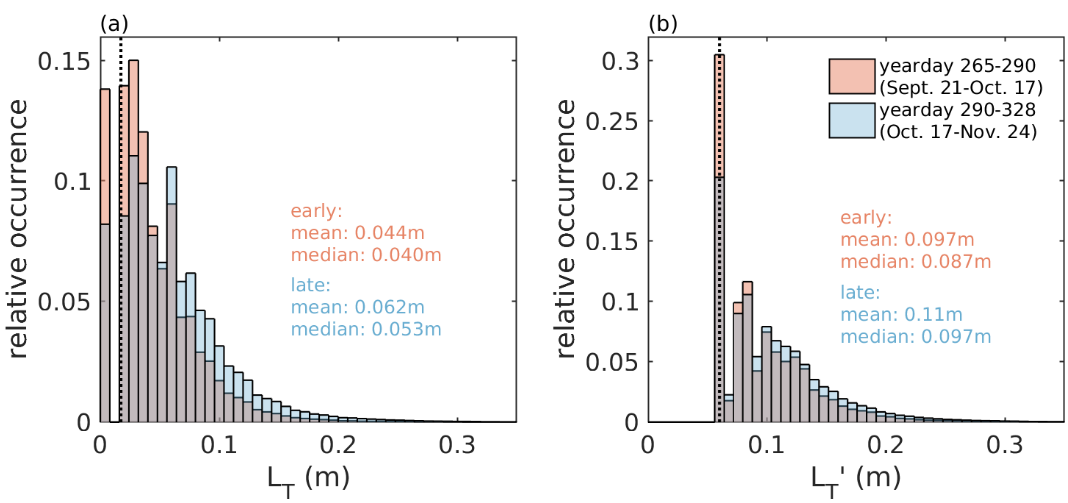

FIG. 8. Distributions of (a) observed values of L_T and (b) non-zero values of L_T' from individual T-chain profiles before and after yearday 290 (pink and blue, respectively). The vertical dashed lines denote the minimum resolvable Thorpe scales, that is, the Thorpe scale corresponding to the case in which the only observed overturn consists of two adjacent measurements.

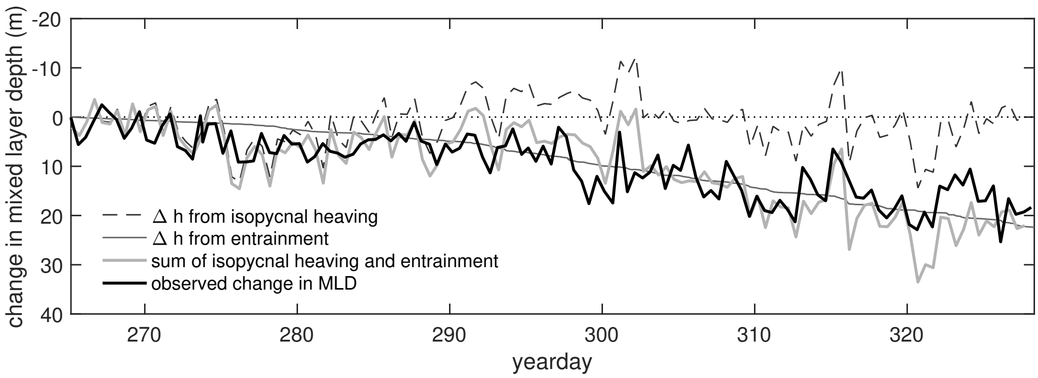

FIG. 9. Change in observed mixed layer depth over the course of the deployment compared with predicted depth evolution based on the estimated entrainment from L_T values and isopycnal heaving (separately and together).

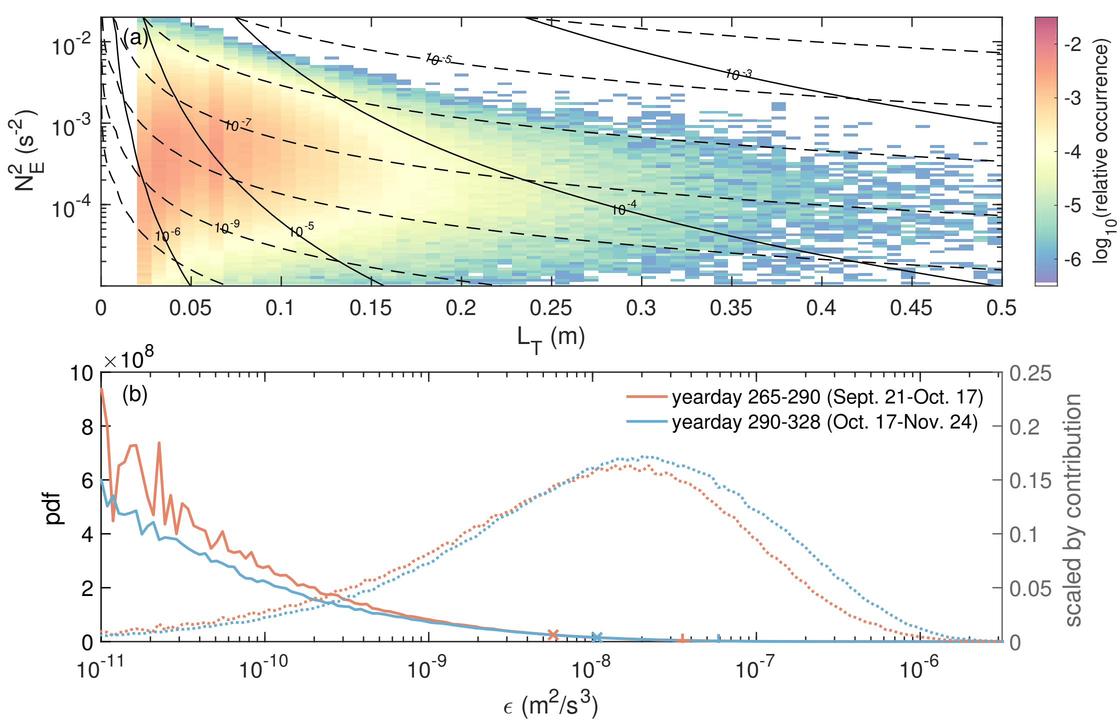

FIG. 10. (a) Distribution of Thorpe scales L_T and weighted stratification N_E^2 (colour). Solid and dashed contours denote the corresponding diffusivities K_E and dissipation rates ε as calculated by equations (14) and (7), respectively. Note that both the stratification bins and the colour scale are logarithmic. (b) Distributions of dissipation rate, ε, at the mixed layer base for the early and late parts of the deployment. Solid lines denote the probability density function, and dotted lines denote the heat flux distributions scaled by contribution to the total dissipation. The $\times$ and + symbols denote the medians and means, respectively.

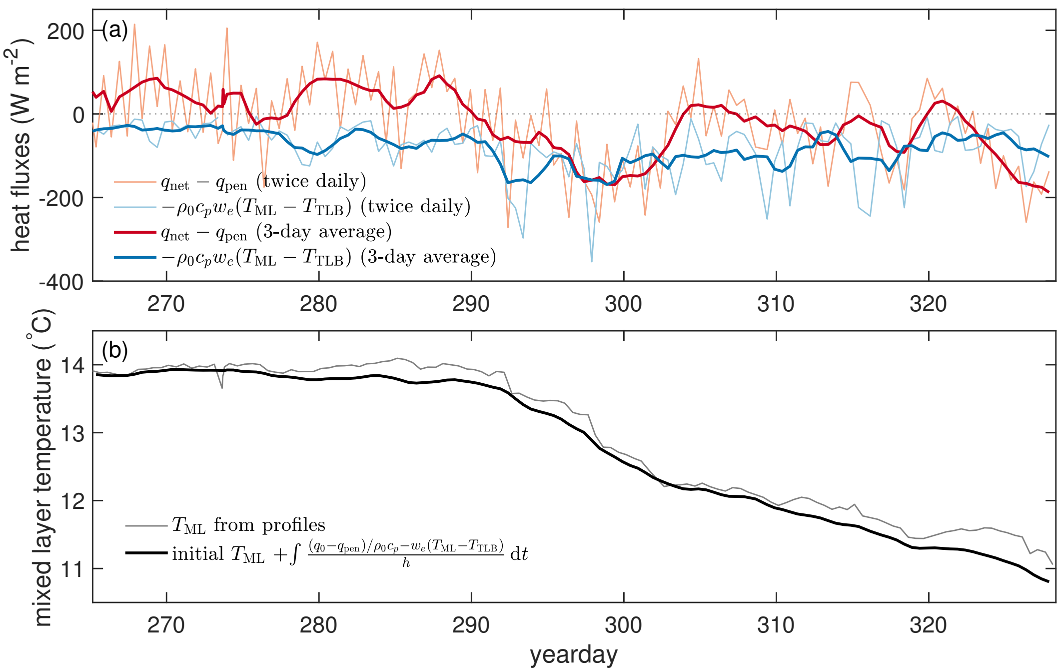

936 FIG. 11. (a) Surface heat fluxes and estimated entrainment fluxes. Thin lines correspond to values averaged between successive twice-daily OSBL profiles and thick lines to a 3-day running average. (b) Observed and predicted evolution of mixed layer temperature $T_{\rm ML}$.

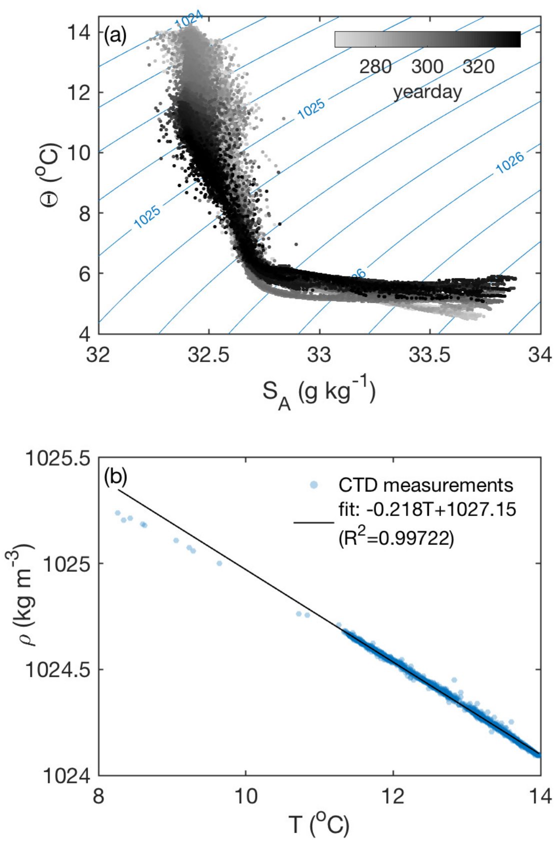

Fig. A1. (a) Conservative temperature Θ and absolute salinity S_A from the CTD measurements for the full deployment. Darker colours denote later dates. Contours show the corresponding potential density referenced to the surface and have an interval of $0.25\,\mathrm{kg\,m^{-3}}$. (b) An example of the fit between the measured CTD temperature T and the computed potential density ρ for the nine-hour Lagrangian drift period between successive profiles on yearday 282-283.

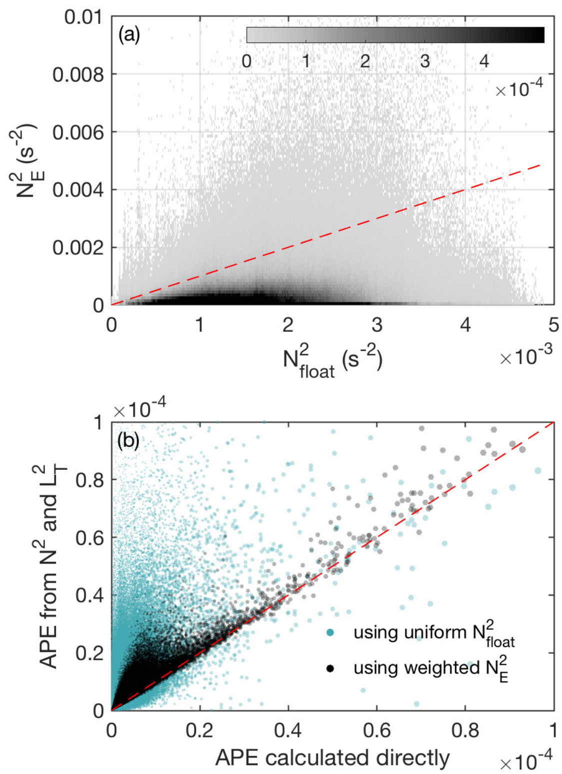

Fig. B1. (a) 2-D histogram of overturn-weighted stratification N_E^2 and corresponding linear fit between the CTDs, N^2_{float}. Colours denote the fraction of observations in a given bin. (b) A comparison of the L_T-based estimate of the available potential energy, APE $\simeq N^2 L_T^2/2$, to the direct estimate given by equation (B1). The blue points correspond to estimates of the APE using a uniform stratification across the body of the float, while the black points correspond to estimates using the weighted bulk stratification N_E. In both panels, the dashed red line indicates the 1:1 line.